# Enhanced laser absorption and ion acceleration by boron nitride nanotube targets and high-energy PW laser pulses

M. Tosca [1,2,3,*] A. Morace,[4] M. Schollmeier [3] S. Steinke,[3] V. Shirvanyan,[3] Y. Arikawa,[4] L. Giuffrida,[1] D. Margarone,[1,5]
P. Pleskunov,[2] A. Choukourov [2] R. R. Whitney,[6] L. R. Scammell [6] and G. Korn[1,3]

[1]*ELI Beamlines Facility, The Extreme Light Infrastructure ERIC, Dolní Brežany 252 41, Czech Republic*
[2]*Charles University, Faculty of Mathematics and Physics, Department of Macromolecular Physics, Prague 180 00, Czech Republic*
[3]*Marvel Fusion GmbH, Theresienhöhe 12, 80339 Munich, Germany*
[4]*Institute of Laser Engineering, Osaka University, 2-6 Yamada-oka, Suita 565-0871, Japan*
[5]*Centre for Light-Matter Interactions, School of Mathematics and Physics, Queen's University Belfast, Belfast BT7 1NN, United Kingdom*
[6]*BNNT Materials, LLC, 300 Ed Wright Lane, Newport News, Virginia 23606, USA*

Enhancing laser energy absorption with energy transfer to fast electrons is crucial for efficient laser-driven ion acceleration. In this work, we present an experimental demonstration of volumetric laser absorption using boron nitride nanotube (BNNT) targets with an average density of $\frac{1}{5}$ of the solid density. We use a PW laser system operating at a pulse duration of 1.2 ps and an energy of 1.3 kJ, reaching intensities of 2×10^{19} W cm^{-2} on target with moderate nanosecond contrast (10^9), to generate energetic ion streams from a 250 μm thick BNNT target. To characterize laser-accelerated ions, Thomson parabola spectrometers, CR-39 nuclear track detectors, and an electron spectrometer are employed. The results are compared to those achieved using flat targets made of polystyrene (PS) of the same thickness. The comparison reveals a 1.5-fold increase in proton maximum energy and a 2.5-fold increase in the maximum energy of heavy ions (C and N) when comparing the BNNT to PS. Moreover, the high-energy ion flux recorded at CR-39 is orders of magnitude higher for the BNNT after cutting off low-energy ions with Al filters. The enhanced ion acceleration is the result of a 2.3-fold increase in the electron temperature for BNNT, as measured by the electron spectrometer. These experimental findings are further validated through two-dimensional particle-in-cell simulations, which confirm the increase in electron temperature due to enhanced laser absorption ascribable to the low density and nanostructure of the BNNT target compared to the flat foil.

I. INTRODUCTION

Laser ion acceleration has been a very active research field for the past two decades and numerous methods and mechanisms have been explored [1,2]. Target normal sheath acceleration (TNSA) is the most experimentally investigated approach and several methods to increase the maximum ion energy and the laser-to-ion energy conversion efficiency have been proposed [3,4]. This mechanism is based on space charge separation between fast electrons, accelerated after laser absorption at the target front side, and ions generated at the target rear surface [5]. The ions accelerated into the vacuum can reach kinetic energies from a few MeV to several tens of MeV depending on the characteristics of the particular laser system [6]. The benefit of laser-driven ion sources resides in their compactness, versatility (various ion species can be accelerated), ultrashort pulse duration, low emittance, and potentially lower costs compared to conventional accelerators. The growing interest in such sources as well as the upcoming laser systems characterized by high repetition rate and high energy (ultimately intensity on target) paves the way towards multidisciplinary applications of societal impact, such as medical proton therapy [7], production of isotopes [8], or cultural heritage investigations [9]. Within all the applications of short-pulse, laser-driven ion acceleration, there is also a branch of studies which investigates the possibility to trigger nuclear fusion reactions in the plasma generated during the interaction [10]. The most studied nuclear fusion reactions triggered with lasers are the ^{2}H(^{3}H; ^{4}He)n [11,12] and the ^{2}H(^{2}H; ^{3}H)n reaction for neutron production (see, e.g., [13–15]) and recently the ^{1}H(^{11}B; ^{4}He)2^{4}He [16–19] reaction for alpha particle production or fusion research. The efficiency of acceleration and hence the laser absorption is mainly due to two factors: the laser beam profile and the target morphology [20]. Thin layers of plasma polymers deposited on top of the targets have been used to increase the coupling in the laser-target interaction [21]. In general, near-critical-density, structured, or unstructured foam targets are used to enhance the energy transfer from the laser pulse to hot electrons and ions. It is well known that structures such
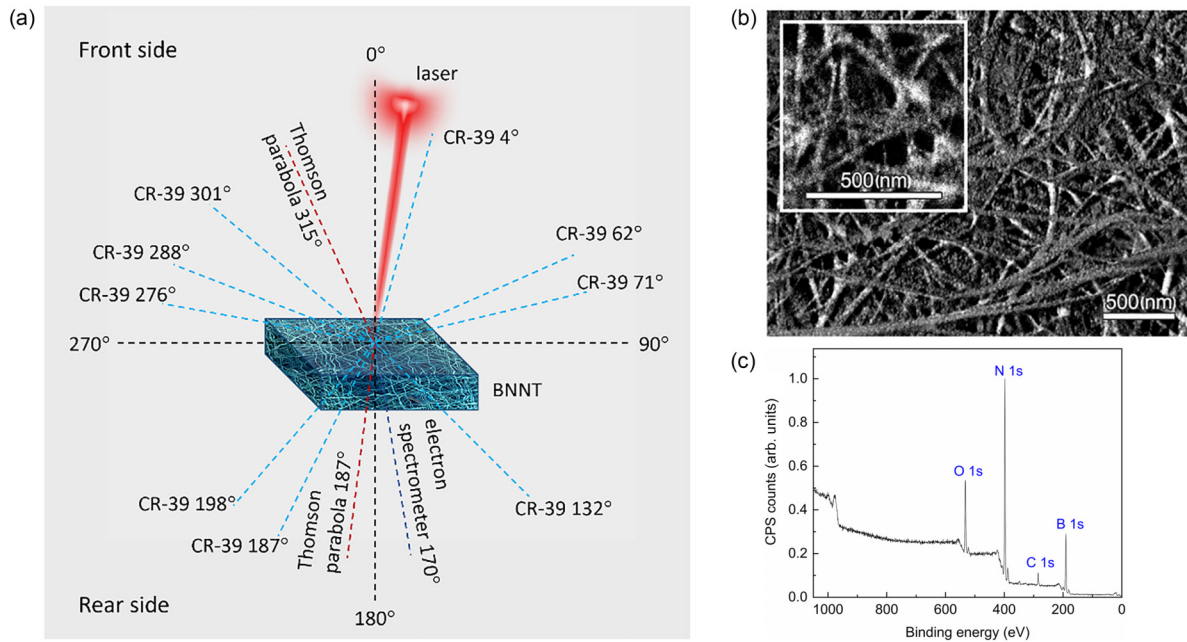
*marco.tosca@eli-beams.eu

FIG. 1. (a) Experimental setup: Two TPs are placed on the front (315°) and the rear side (180°) and an electron spectrometer is placed next to the TP at the rear side at a distance of 120 cm from the interaction point. Ten CR-39's were placed at different angles and distances from the interaction point. The CR-39's were covered with Al filters of different thicknesses with a custom 3D printed holder. (b) The top-view SEM micrographs of the BNNT sample with various magnifications: $40\,000\times$ (main) and $75\,000\times$ (inset). (c) The XPS wide spectrum of the BNNT sample.

as nanowires can absorb laser pulse energies with efficiency of up to ~80% [22,23]. Other experiments investigating the performance of different micro- to nanostructured foam layers were conducted in [24,25] resulting in a 10-fold higher proton flux and a 2-fold higher cutoff energy compared to standard flat targets [26]. Nanostructured layers placed on the front or rear side of the target, besides the higher cutoff energy and higher flux, can also modify the trajectory and the divergence of the emitted particles [27,28].

In this work, we study the ion emission generated by the kJ PW, picosecond Laser for Fast Ignition Experiments (LFEX) at the Institute of Laser Engineering (ILE) in Osaka, Japan [29], through the interaction with near-solid-density boron nitride nanotube targets (BNNTs) provided by "BNNT Materials" (Newport News, USA). The objective was to achieve more efficient acceleration, both in terms of energy and flux, of protons and ions using a single-shot PW laser without the requirement for high contrast typically implying the use of plasma mirrors and, thus, reducing the laser energy on the target. The results achieved with the BNNT targets were compared with those measured with standard flat foil targets made of polystyrene (PS).

II. MATERIALS AND METHODS

A. Experimental setup

1. Laser

The LFEX laser system delivers 1.3 kJ of energy in a 1.2 ps pulse at the fundamental wavelength of 1.053 μm, capable of reaching a maximum intensity of 2×10^{19} W cm^{-2} on target. A schematic representation of the experimental setup is shown

in Fig 1(a). The front target normal is set as 0° and the angles are counted clockwise. The laser beam, depicted in red, was focused to a 50 μm diameter focal spot at full width at half maximum (FWHM), interacting with the target's front surface at an angle of 7°.

2. Target types and characterization

BNNTs were synthesized by a high-temperature and pressure (HTP) process, also referred to as the pressurized vapor/condenser method, in which boron is brought to a liquid state in a pressurized nitrogen atmosphere [30]. Boron was isotopically purified with an over 98 at. % yield of boron-11. The BNNTs were refined and partially purified to remove boron particles and non-nanotube BN impurities; the resultant material contained >75 wt % of nanotubes. Consequently, the BNNT material was dispersed in an alcohol solution and lyophilized to make a powder. Aliquots of powder were compressed into pellets of 250 μm thickness and with an average density of ~0.5–1.0 g cm^{-3}.

The morphology of the BNNT sample was studied using scanning electron microscopy (SEM). A 2 nm thin film of Au was deposited on the surface prior to the measurements to improve the surface conductivity and the quality of the images. The observations were conducted in a top-view geometry. Figure 1(b) shows the SEM images of the BNNT sample surface at two magnifications, revealing a porous structure consisting of the nanotubes with lengths ranging from 1 μm to hundreds of μm and diameters of individual nanotubes and bundles up to tens of nm.

X-ray photoelectron spectroscopy (XPS) was used to probe the elemental composition of the BNNTs [Fig. 1(c) and

TABLE I. Elemental content of the BNNT sample.

B (at. %)	C (at. %)	N (at. %)	O (at. %)
43.5	4.7	40.0	11.8

Table I], confirming that the BNNTs consist of stoichiometric boron nitride. Small contributions from C and O are associated with impurities from the ambient atmosphere. For reference, a polystyrene foil with a thickness of 250 μm was used as a control target to evaluate the laser-target interaction.

3. Particle diagnostics

To detect the products resulting from the laser-target interaction and their corresponding energy distributions, multiple diagnostic tools were employed. These include Thomson parabola spectrometers (TPs), an electron spectrometer, and CR-39 nuclear track detectors covered with aluminum filters ranging from 6.5 to 70 μm in thickness [31].

The TPs were positioned at 187° and 315° to measure ions emitted from the rear and front sides of the target, respectively. The TPs allow for the differentiation of various ion species and the reconstruction of their energy distribution. It should be noted that ions with the same charge-to-mass ratio (q/M) may produce overlapping traces on the detector.

CR-39 detectors were placed in the experimental chamber at intervals of approximately 30°. After the irradiation, the CR-39 detectors were etched in a concentrated basic solution (6.25 M NaOH at 70 °C for 30 min) to enlarge the latent tracks to the micron scale. The dimensions of the visible tracks are proportional to the energy deposited during the irradiation process. It is important to mention that the minimum radiation damage density required for detection corresponds to the point at which the etching solution can penetrate the crater and enlarge its size.

In this study, ion emissions from light particles ($Z < 3$) are neglected due to limitations in both the etching conditions and the spatial resolution of our digitization microscope. This limitation has been confirmed in earlier calibrations conducted under similar experimental conditions [32].

The electron spectrometer, situated on the rear side of the target at an angle of 170°, employs a magnetic field to bend a beam of incoming electrons formed by a pinhole at the front of the diagnostic. The deflection of the electron beam is inversely proportional to its energy. An imaging plate (IP) of Fuji BAS-MS type was used at the detector plane to measure the electron spectrum.

III. RESULTS AND DISCUSSION

A. Thomson parabola spectrometer

As previously described, we employed two Thomson parabola spectrometers (TPs) to analyze the ion emission resulting from the laser-driven process. Figures 2(a) and 2(b) represent the raw TP traces obtained during the experiment,
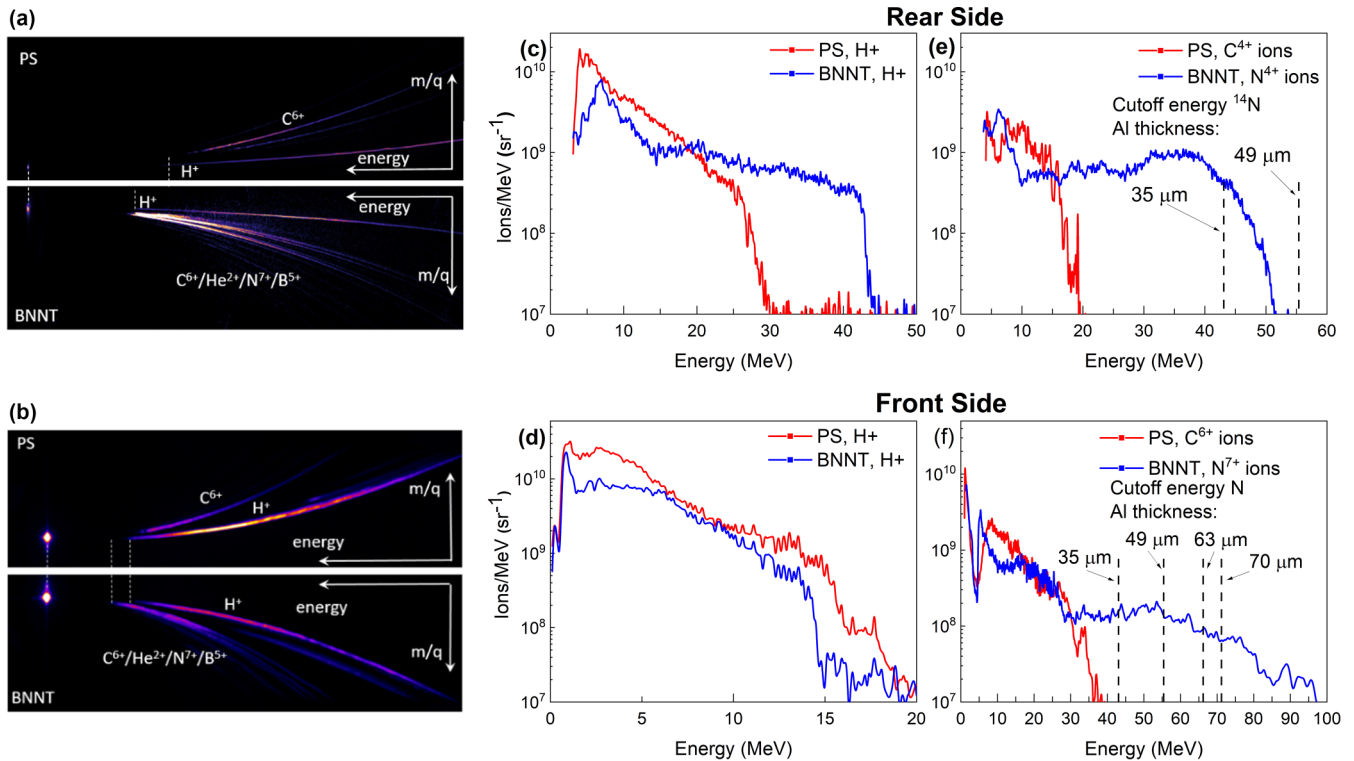

FIG. 2. TP energy distribution for both BNNT and PS: (a) Raw parabola traces on the image plate for PS and in a mirror image the BNNT for the TP placed at 187° (rear side) and (b) for the TP placed at 315° (front side). The images are plotted on the same color scale. The dashed vertical lines plot the position of the origin (left side) and the cutoff energies for protons. (c) Energy distribution of protons from the rear side and (d) from the front side. (e) Energy distribution of C and N with cutoff energy of N using 35 and 49 μm Al thickness from the rear side and (f) with cutoff energy of N using 35, 49, 63, and 70 μm Al thickness from the front side to compare with the CR-39 results.

showcasing results for the PS target (top part) and the BNNT target (bottom part), for ions emitted from the rear and front sides, respectively. For visual comparison, the top part of each figure displays parabolas obtained from the reference PS targets, while the bottom part exhibits parabolas from the BNNT targets. These raw data were then used to reconstruct energy distributions for various ion species. Note that C^{4-5+}, N^{4-5+}, and B^{4+} ions are hardly distinguishable in the m/z traces of TPs; however, it is logical to assume that the signal from the BNNT is enriched by N and B ions, while the signal from PS comes from C ions. In our analysis, we factored in both the N and C comparisons for reference.

Figures 2(c) and 2(d) present the proton spectra obtained from the rear and front sides, respectively. Additionally, Figs. 2(e) and 2(f) display the energy distributions for C and N ions on the rear and front sides.

At the rear side, protons emitted from the BNNT target exhibited a maximum energy of 45 MeV, whereas the PS target showed a maximum energy of 30 MeV. Consequently, BNNTs demonstrated a 1.5 times higher proton maximum energy compared to the reference PS target [Fig. 2(c)]. Figure 2(e) illustrates the energy distribution for C^{4+} ions from the PS target and N^{4+} ions from the BNNT target at their rear sides. These ions have close values of m/z; however, the spectra indicate maximum energies of 20 MeV for C^{4+} (PS) and 51 MeV for N^{4+} (BNNT), resulting in a 2.5 times higher maximum energy for BNNT. Furthermore, in addition to the variation in maximum ion energy, there is also an alteration in spectral shapes for different ions. Specifically, in the case of BNNT, the proton spectrum exhibits a faster decay at higher energies compared to the PS spectrum while for the signals from C and N the decay is comparable.

On the front side, the TP recorded proton distributions similar for BNNT and PS, with cutoffs at approximately 20 MeV [Fig. 2(d)]. However, C^{6+} and N^{7+} ions also exhibited a 2.5-fold increase compared to the rear side, with energies of 38 and 96 MeV, respectively [Fig. 2(f)]. To correlate the signal present on the TPs and the ion flux measured on the CR-39, the cutoff energy of N ions for different Al thickness is implemented in the spectra in Figs. 2(e) and 2(f).

As will be further demonstrated by the electron spectra, the higher ion cutoff energies observed for BNNTs are likely attributed to enhanced laser absorption within the nanostructured bulk, resulting in higher electron temperatures and densities, consequently leading to more efficient ion acceleration compared to an unstructured foil target. Several factors may contribute to the higher absorption in the nanostructured targets. The nanotube's front side effectively provides a larger surface area for the incident laser pulse, enabling a greater number of atoms to interact with the laser field [28]. Moreover, the nanotubes, resembling a foamlike structure, are intertwined, yielding an overall thickness of 250 μm. In this configuration, when the laser impinges upon these structures, the pulse can permeate through the nanotubes, resulting in enhanced laser energy absorption [24]. The cumulative effects are evident in the increased ion energies observed. Further discussions concerning absorption mechanisms will be presented in the following simulation section.

B. CR-39 detector measurements

The TPs used in this experiment were previously calibrated for energy using aluminum (Al) filters on the image plate. However, they cover only two small regions of the solid angle. To overcome this issue, we positioned CR-39 detectors at various locations around the interaction point, exploring ion emissions at ten different angles and distances. The detectors were placed at distances of 85 cm, such as on the chamber wall, and at 145 cm when using extension tubes.

The used holders for the CR-39s were made of six separate compartments, which were facing the interaction point and were covered by Al filters of different thicknesses (6.5, 14, 35, 49, 63, and 70 μm). As the thickness of the filter increases, there is a significant reduction in the number of particles that manage to pass through. The Al essentially functions as a high-pass filter because ions with energies falling below the stopping range in the Al do not penetrate through the foil. This property enables the sampling of distinct segments of the ion spectra. The corresponding cutoff energy for the ^{1}H, ^{11}B, ^{12}C, and ^{14}N ions was calculated for each filter using LISE++ [33] and shown in Table II.

Figure 3 presents a summary of the results obtained using the CR-39 detectors, while Tables S1 and S2 of the Supplemental Material provide the complete data set [34]. The unexpectedly strong emission from the BNNTs caused detector saturation with Al filters thinner than 49 μm (6.5, 14, and 35 μm); therefore, only data for BNNTs with thick Al filters (49, 63, and 70 μm) can be of use. On the contrary, the CR-39 detectors used with the PS target gave reliable results for thin Al filters but produced minimal signals for thicknesses of 63 and 70 μm. Thus, only the 49 μm Al filter data are available for detailed comparison between BNNT and PS.

Figures 3(a) and 3(b) provide a comparison of the pit area distributions and ion fluxes obtained from the CR-39 detectors covered with 49 μm thick Al filters and positioned on the front side at 300° and at a distance of 145 cm from the interaction point. Representative images of these detectors are shown as insets for a direct visual comparison of the differences. The ion flux for PS was 7.58×10^8 ions sr^{-1}, whereas for BNNT it reached 5.04×10^{10} ions sr^{-1}, resulting in a 65-fold increase. Note that the background level was estimated to be at 6.00×10^6 ions sr^{-1} and therefore the provided values are relevant. It should also be emphasized that different ensembles of ions with different energy distributions are involved in both cases: N and B are the most abundant elements in BNNT, while C and H are characteristic for PS. Table II demonstrates that 49 μm Al passes B > 39.9 MeV and N > 55.4 MeV for BNNT, and H > 2.2 MeV and C > 44.3 MeV for PS. Since the CR-39 detectors lack specific calibration for heavy ions such as boron, carbon, or nitrogen, distinguishing them according to the track size is not feasible. Consequently, the observed increase in the ion flux is related to all ion species with energies above the 49 μm Al filter cutoff.

Figure 3(c) illustrates the angular distribution of the ion emission detected by all CR-39 detectors present in the experimental chamber. The same trend can be observed in all positions, pointing to a higher total ion flux for BNNT compared to that for PS. In the ultimate case of a rear cone of

TABLE II. Cutoff energy (MeV) of the ions involved for Al with different thicknesses.

Ion	Aluminum thickness					
	6.5 (µm)	14.0 (µm)	35.0 (µm)	49.0 (µm)	63.0 (µm)	70.0 (µm)
^{1}H	0.6	1.0	1.8	2.2	2.6	2.8
^{11}B	5.7	12.7	27.3	34.9	41.6	44.7
^{12}C	7.3	16.2	34.7	44.3	52.9	56.8
^{14}N	8.8	19.9	43.2	55.4	66.2	71.2

approximately 30°, where electrons are more energetic and abundant, the BNNTs exhibited an ion emission of 4.67×10^{10} ions sr^{-1}, while PS showed 7.16×10^7 ions sr^{-1} (cf. results at 187° for a 49 µm Al filter). As a result, we measure a 650 times higher total ion flux for the BNNT than for PS in this case. The fluxes recorded closer to 90° and 270° show a smaller difference, which nevertheless constitutes about an order of magnitude.

This is a significant enhancement that we recorded. Previous research, albeit with different laser parameters, reported an enhanced TNSA by a factor of 2 for proton cutoff energy and 4 in proton flux above 4.7 MeV. Notably, this study achieved enhanced TNSA without the use of a plasma mirror, which was a prerequisite in previous investigations involving nanostructured targets [22,24].

The comparable thickness of the PS and BNNT targets enables a meaningful comparison of the underlying physics governing the acceleration mechanisms. It is evident that the energy absorption by BNNTs significantly surpasses that of flat PS targets. This surplus energy efficiently transfers to ions, resulting in enhanced TNSA. Our CR-39 results match the findings of the TP. Specifically, we observe a clear enhancement in the total ion flux for BNNTs compared to PS.

C. Electron spectrometer and simulations

The results from the electron spectrometer are shown in Fig. 4 for reference PS target and a BNNT target. The mean temperature of the hot electrons T_e was calculated by fitting a distribution with an exponentially decaying function $N(E) = N_0 \exp(\frac{-E}{k_B T_e})$ [3], where $k_B T_e$ is the electron temperature and k_B is the Boltzmann constant. The PS spectrum is very smooth and can be described by a single temperature, typical of ponderomotive forces [35]. In contrast, the BNNT spectrum shows pronounced modulation that we divide into two regions. From 0 to 2 MeV the spectrum has a pronounced decay while above 2 MeV the spectrum can be approximated by a constant slope. The obtained temper-
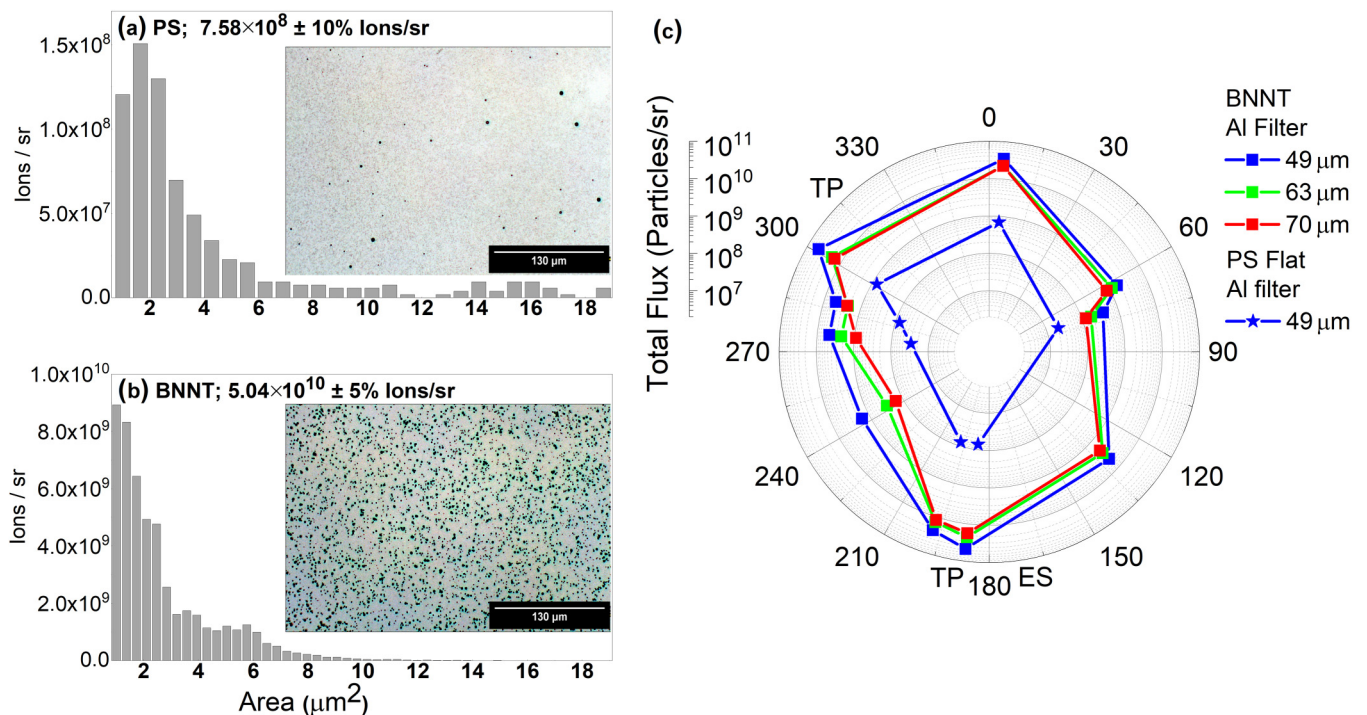

FIG. 3. Total ion fluxes obtained from BNNT and PS targets using CR-39 detectors: (a), (b) pit area distributions obtained using PS and BNNT targets behind the 49 µm thick Al filter and placed at 300° from the target normal; insets show photo examples of CR-39 detectors (note the two orders of magnitude higher ion counts for the BNNT). (c) Angular distribution of the total ion flux recorded by CR-39 using 49, 63, and 70 µm Al filters for BNNTs and 49 µm Al filter for PS (PS does not show measurable fluxes using 63 and 70 µm filters in many positions). Each histogram and flux value is based on the mean of ten randomly selected detector images.
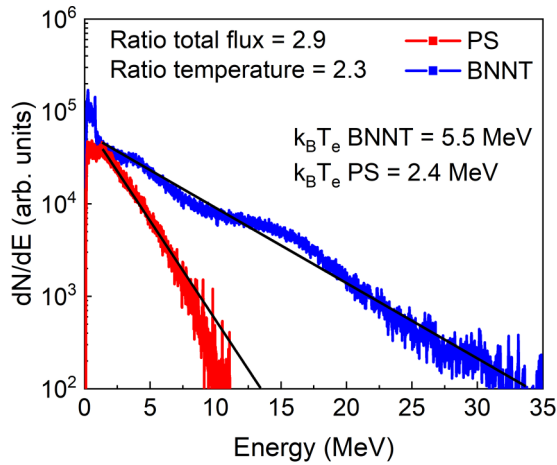
FIG. 4. Electron energy distribution. The BNNT generates electrons up to 33 MeV, while the PS produces up to 11 MeV electrons. The T_e and total flux are 2.3 and 2.9 times higher for BNNT compared to the reference PS.

atures were 2.4 and 5.5 MeV, respectively, for PS and BNNT targets, resulting in a ratio of 2.3 times higher temperature for the BNNT. The flux in both cases was obtained by in-

tegrating the energy distribution, resulting in a ratio of 2.9 between BNNTs and PS. The cutoff energy reaches 33 MeV for BNNT and 11 MeV for PS, which is also three times different.

To understand the physics behind the enhanced laser energy absorption into hot electrons for the BNNT target, we performed 2D collisionless particle-in-cell simulations using the code EPOCH2D [36]. The BNNT target was modeled as a bidimensional cross section along the perpendicular to the laser axis of the BNNT target structure. The BNNT target was composed of nanotubes that were either freestanding or clumped together in larger structures by mechanical compression during target preparation. The resulting structure was composed of larger clumps and smaller tubes separated by vacuum with a cumulative density of 25% of solid BN. A longitudinal cross section of such target would appear as larger and smaller disks separated by vacuum as represented in Fig. 5(a), which shows the initial setup of the simulation, where we randomly generated the target structure while maintaining a realistic target density.

Simulations were performed with a resolution of $\lambda/33$ where λ is the wavelength of the laser of 1054 nm and open boundaries for both particles and fields on all sides of the simulation box. To collect the relativistic electrons, we used
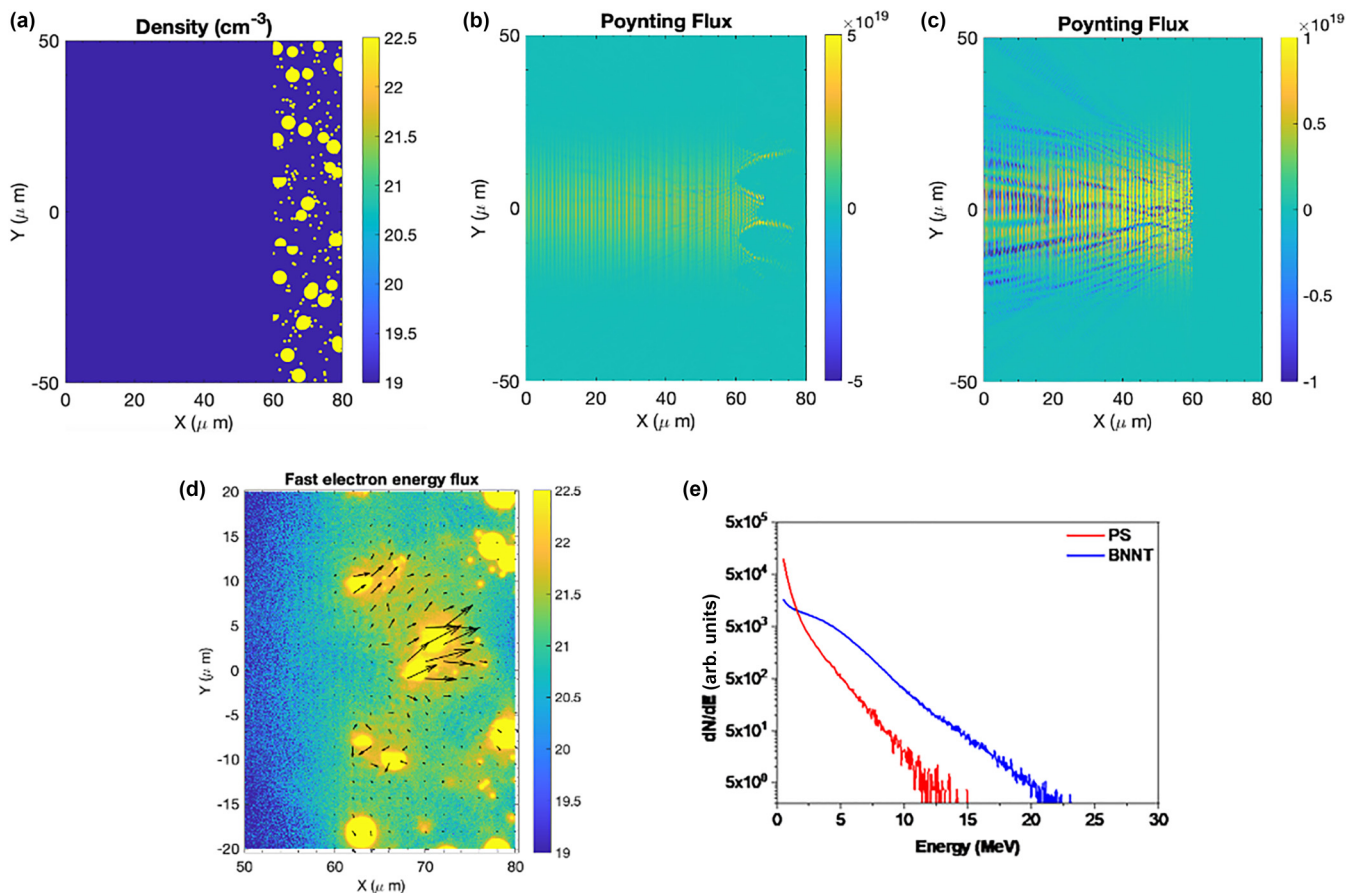

FIG. 5. (a) Modeling of the BNNT target input for EPOCH2D simulations. The BNNT target starts at $x = 60\,\mu m$ and is composed of micron or nm-sized disks at random locations as described in the text. The laser pulse enters the box from the left side at $x = 0$ and propagates in vacuum until it interacts with the target. (b) Poynting flux after the main peak of the laser arrives at the initial BNNT target front surface and (c) the same for a flat PS target. (d) Simulated fast electron energy flux contribution corresponding to (b). (e) Resulting electron energy distribution for BNNT target (blue) and PS target (red) at the end of the simulation runs.

an extraction plane normal to the x axis set at 75 μm in the simulation box. This diagnostic is recording the momentum components of all electrons that cross it with positive p_x momentum, which means the electrons moving towards the laser focus are not considered.

Since both boron and nitrogen are fully ionized in the laser-plasma interaction region as evidenced by the TP traces, for simplicity we replaced the two species with deuterium, which has the same charge-to-mass ratio, and the plasma dynamics is therefore maintained. The initial plasma density was set to 50 times the critical density (n_c) and the peak laser intensity on the target was set at 1.3×10^{19} W cm^{-2}, which corresponds to the estimated LFEX intensity on target. Simulation results for this target are compared to those of a simple deuteron flat foil at 50 n_c density.

Given the fairly good LFEX contrast during normal operation [37], the simulations were conducted in the absence of preformed plasma (for both cases) due to the extreme complexity of simulating the action of a very low intensity laser pedestal on the BNNT target. We believe this to be a reasonable compromise since the most relevant physics occurs during the main pulse interaction.

From the simulation results we can identify two main processes responsible for the laser energy absorption enhancement in the BNNT target: (i) the rapid explosion of the smaller size tubes (disks) during laser irradiation that leads to the formation of a near critical density plasma, and (ii) the persistence of the larger clumps that act as a microstructured target.

The nanotubes explode within 600 fs from the initial laser irradiation of the target, leading to the formation of a near-critical-density plasma before the laser peak intensity reaches the target. The laser pulse undergoes self-focusing in the plasma, thus increasing the laser intensity by almost an order of magnitude and leading to the generation of hotter electrons compared to the PS target. Figure 5(b) shows the x component of the Poynting flux and we can clearly appreciate the enhancement in laser intensity due to laser beam self-focusing. We do not observe back-reflected or backscattered light (visible by a negative pointing flux), which is a sign that most laser energy is absorbed in the plasma, while on the contrary for the simple flat foil we can observe a significant fraction of backscattered light [see Fig. 5(c)]. The stronger backscattered light for the foil target confirms that a smaller fraction of the laser energy is absorbed and converted into hot electrons.

Finally, the larger clumps act as a microstructured target, significantly increasing the laser-to-electron energy conversion efficiency via vacuum-heating/Brunel effect type mechanisms. In Fig. 5(d) we show the net fast electron energy flux (the black arrows) superimposed to the plasma density, clearly indicating that the majority of the hot electrons are generated at the high-density plasma clumps in the laser plasma interaction region.

The combined action of higher laser intensity due to self-focusing and enhanced laser energy absorption at the surviving microstructures results in the generation of a larger number of hotter electrons compared to the simple foil case. Figure 5(e) shows that the electron energy distribution is

shifted to higher energies in the case of BNNTs as compared to PS. Additional simulations were performed on PS with low density corresponding to the average density of the BNNT target (Fig. S1 of the Supplemental Material [34]). They did not find significant changes in the electron energy distributions between the high-density and low-density PS, providing evidence that the average density of the target is not the crucial parameter that leads to the enhanced TNSA.

IV. CONCLUSIONS

The LFEX interaction with the BNNT targets results in enhanced laser energy absorption, higher electron and ion fluxes, and higher electron and ion cutoff energies compared to flat PS targets. The BNNT targets consist of nanotubes with diameters between 2 and 100 nm and their bundles. The TP and the electron spectrometer registered the enhanced TNSA on the rear side of the target resulting in the 1.5-fold proton maximum energy and 2.5-fold maximum energies of heavy ions (C^{4+} and N^{4+}). The CR-39 confirmed the results with an increment of two orders of magnitude in $Z > 2$ ion flux for energies above the cutoff energy set by the 49 μm Al filter and the electron spectrometer also confirmed the same trend for electrons resulting in $3\times$ cutoff energy, $2.9\times$ in flux and $2.3\times$ in hot electron temperature. The 2D simulations, in particular the Poynting flux, show a longer propagation of the main pulse that allows the self-focusing effect to efficiently develop, also supported by the explosion of the smaller nanotubes prior to the laser peak's arrival (generation of near-critical-density background plasma for a more efficient laser coupling). Furthermore, the presence of microstructures alternated with empty pockets improves the energy absorption into hot electrons, thus the overall hot electron flux. Such enhanced TNSA regime using nanostructured targets is demonstrated experimentally using PW-level kJ-level laser pulses both for protons and heavier ions (C and N).

Our experimental findings highlight the potential of BNNT targets in terms of efficient energy transfer during laser-matter interaction at relativistic intensities using high-energy laser pulses with implications for potential use of such particle source for applications requiring high flux, especially in the case of heavy ions. The unique elemental composition of the target, rich in boron-11, also opens avenues for exploring the proton-boron nuclear fusion reaction and its optimization using the in-target scheme, which will require a volumetric laser-target coupling.

[1] H. Daido, M. Nishiuchi, and A. S. Pirozhkov, Review of laser-driven ion sources and their applications, Rep. Prog. Phys. **75**, 056401 (2012).

[2] G. A. Mourou, C. L. Labaune, M. Dunne, N. Naumova, and V. T. Tikhonchuk, Relativistic laser-matter interaction: From attosecond pulse generation to fast ignition, in *Plasma Physics and Controlled Fusion*, Vol. 49 (IOP Science, Bristol, UK, 2007).

[3] A. Macchi, M. Borghesi, and M. Passoni, Ion acceleration by superintense laser-plasma interaction, Rev. Mod. Phys. **85**, 751 (2013).

[4] S. C. Wilks, A. B. Langdon, T. E. Cowan, M. Roth, M. Singh, S. Hatchett, M. H. Key, D. Pennington, A. MacKinnon, and R. A. Snavely, Energetic proton generation in ultra-intense laser-solid interactions, Phys. Plasmas **8**, 542 (2001).

[5] S. P. Hatchett *et al.*, Electron, photon, and ion beams from the relativistic interaction of Petawatt laser pulses with solid targets, Phys. Plasmas **7**, 2076 (2000).

[6] M. Zimmer, S. Scheuren, T. Ebert, G. Schaumann, B. Schmitz, J. Hornung, V. Bagnoud, C. Rödel, and M. Roth, Analysis of laser-proton acceleration experiments for development of empirical scaling laws, Phys. Rev. E **104**, 045210 (2021).

[7] S. V. Bulanov and V. S. Khoroshkov, Feasibility of using laser ion accelerators in proton therapy, Plasma Phys. Rep. **28**, 453 (2002).

[8] K. W. D. Ledingham *et al.*, High power laser production of short-lived isotopes for positron emission tomography, J. Phys. D: Appl. Phys. **37**, 2341 (2004).

[9] M. Barberio, S. Veltri, M. Sciscic, and P. Antici, Laser-accelerated proton beams as diagnostics for cultural heritage, Sci. Rep. **7**, 40415 (2017).

[10] V. S. Belyaev, A. P. Matafonov, V. I. Vinogradov, V. P. Krainov, V. S. Lisitsa, A. S. Roussetski, G. N. Ignatyev, and V. P. Andrianov, Observation of neutronless fusion reactions in picosecond laser plasmas, Phys. Rev. E **72**, 026406 (2005).

[11] A. B. Zylstra *et al.*, Burning plasma achieved in inertial fusion, Nature (London) **601**, 542 (2022).

[12] ITER demo, accessed May 14, 2023. Available at https://www.iter.org/proj/inafewlines

[13] J. Krása and D. Klír, Scaling of laser fusion experiments for DD-neutron yield, Front. Phys. **8**, 310 (2020).

[14] A. Curtis *et al.*, Ion acceleration and D-D fusion neutron generation in relativistically transparent deuterated nanowire arrays, Phys. Rev. Res. **3**, 043181 (2021).

[15] A. Curtis *et al.*, Micro-scale fusion in dense relativistic nanowire array plasmas, Nat. Commun. **9**, 1077 (2018).

[16] C. Labaune *et al.*, Fusion reactions initiated by laser-accelerated particle beams in a laser-produced plasma, Nat. Commun. **4**, 2506 (2013).

[17] L. Giuffrida *et al.*, High-current stream of energetic α particles from laser-driven proton-boron fusion, Phys. Rev. E **101**, 013204 (2020).

[18] M. S. Schollmeier *et al.*, Differentiating multi-MeV, multi-ion spectra with CR-39 solid-state nuclear track detectors, Sci. Rep. **13**, 18155 (2023).

[19] D. Margarone *et al.*, In-target proton–boron nuclear fusion using a PW-class laser, Appl. Sci. **12**, 1444 (2022).

[20] M. Kaluza, J. Schreiber, M. I. K. Santala, G. D. Tsakiris, K. Eidmann, J. Meyer-ter-Vehn, and K. J. Witte, Influence of the laser prepulse on proton acceleration in thin-foil experiments, Phys. Rev. Lett. **93**, 045003 (2004).

[21] M. Tosca *et al.*, Plasma polymers as targets for laser-driven proton-boron fusion, Front. Phys. **11**, 1227140 (2023).

[22] J. Park *et al.*, Absolute laser energy absorption measurement of relativistic 0.7 ps laser pulses in nanowire arrays, Phys. Plasmas **28**, 023302 (2021).

[23] J. H. Bin *et al.*, Enhanced laser-driven ion acceleration by super-ponderomotive electrons generated from near-critical-density plasma, Phys. Rev. Lett. **120**, 074801 (2018).

[24] I. Prencipe *et al.*, Efficient laser-driven proton and bremsstrahlung generation from cluster-assembled foam targets, New J. Phys. **23**, 093015 (2021).

[25] O. Klimo *et al.*, Short pulse laser interaction with micro-structured targets: Simulations of laser absorption and ion acceleration, New J. Phys. **13**, 053028 (2011).

[26] M. S. Schollmeier *et al.*, Investigation of proton beam-driven fusion reactions generated by an ultra-short petawatt-scale laser pulse, Laser Part. Beams **2022**, 1 (2022).

[27] L. Giuffrida *et al.*, Manipulation of laser-accelerated proton beam profiles by nanostructured and microstructured targets, Phys. Rev. Accel. Beams **20**, 081301 (2017).

[28] D. Margarone *et al.*, Laser-driven proton acceleration enhancement by nanostructured foils, Phys. Rev. Lett. **109**, 234801 (2012).

[29] A. Morace *et al.*, Enhancing laser beam performance by interfering intense laser beamlets, Nat. Commun. **10**, 2995 (2019).

[30] M. W. Smith *et al.*, Very long single-and few-walled boron nitride nanotubes via the pressurized vapor/condenser method, Nanotechnology **20**, 505604 (2009).

[31] T. W. Jeong *et al.*, CR-39 track detector for multi-MeV ion spectroscopy, Sci. Rep. **7**, 2152 (2017).

[32] V. Kantarelou *et al.*, A methodology for the discrimination of alpha particles from other ions in laser-driven proton-boron reactions using CR-39 detectors coupled in a Thomson parabola spectrometer, Laser Part. Beams **2023**, 1 (2023).

[33] M. P. Kuchera, O. B. Tarasov, D. Bazin, B. Sherril, and K. V. Tarasova, LISE++ software updates and future plans, J. Phys.: Conf. Ser. **664**, 072029 (2015).

[34] See Supplemental Material at http://link.aps.org/supplemental/10.1103/PhysRevResearch.6.023326 for complete data set obtained using CR-39 detector and PIC simulation performed using PS target with average density of the BNNT target.

[35] B. Quesnel and P. Mora, Theory and simulation of the interaction of ultraintense laser pulses with electrons in vacuum, Phys. Rev. E **58**, 3719 (1998).

[36] C. Brady, K. Bennett, H. Schmitz, and C. Ridgers, An open source PIC code for high energy density physics Users Manual for the EPOCH PIC codes, 2014.

[37] N. Miyanaga *et al.*, Technological challenge and activation of 10-kJ PW laser LFEX for fast ignition at ILE, in *Frontiers in Optics 2008/Laser Science XXIV/Plasmonics and Metamaterials/Optical Fabrication and Testing* (OSA, Washington, D.C., 2008), p. FWQ1.